Materials Advances

ROYAL SOCIETY OF CHEMISTRY

PAPER

View Article Online
View Journal | View Issue

Cite this: *Mater. Adv.*, 2025, **6**, 4905

An MoS_2/PEDOT:PSS-based flexible NIR-responsive soft actuator†

Raksha D. Salian,[a] Avijit Kumar Das [b] and Partha Kumbhakar *[a]

Received 5th April 2025,
Accepted 5th June 2025

DOI: 10.1039/d5ma00329f

rsc.li/materials-advances

The development of sophisticated smart devices heavily relies on flexible soft actuators combined with near infrared (NIR) light responsive two-dimensional (2D) materials. Soft robots provide a number of benefits, such as flexibility, high sensitivity, compliance and security. Amidst many manufacturing and driving approaches, light has surfaced as a facilitator, aiding in the fabrication of soft actuators. Using few-layered molybdenum disulphide (MoS_2) and poly(3,4-ethylenedioxythiophene)/poly(styrene sulfonate) (PEDOT:PSS), the current work aims to introduce a polymer nanocomposite film for soft actuator applications under NIR light exposure. The actuation behavior was impacted by PEDOT:PSS under NIR light exposure. In order to incorporate controllable deformation of the actuator, the photothermal properties of the composite film were investigated. *In situ* Raman spectroscopy and the density functional theory (DFT) calculation explain the structural change and energy optimization of PEDOT:PSS. A soft insect was further designed based on this photothermal property, which can deform under light exposure. Therefore, such flexible design has huge potential for soft robotics applications in modern technologies.

Introduction

Actuators have enormous promise for use in biomedicine, electronic skin, and soft robotics because they make it possible to transform the energy of external inputs into mechanical deformation.[1–3] Traditional robots can either move or rotate, which limits their flexibility when interacting with the natural world. Soft actuators enable soft robots to bend, absorb touch, and impact energy differently than rigid robots, which generally work with barriers through deformation.[4] The flexible actuator, a crucial component of soft robotics, primarily produces mechanical energy from heat, light, and electricity, when stimulated, much like the human body "effector".[5,6] Polymer based soft actuators react to a variety of environmental stimuli, including heat, light, moisture, solvent vapor, mechanical and electrical stimuli.[7,8] Among the different kinds of stimuli, optical stimuli are the most straightforward and practical, and photothermal polymers are widely used, which have several advantages over traditional methods like wavelength selection, wireless control, and an abundance of light sources, because they allow for intensity control and customizable light source area.[9] To produce rapid, sensitive, and significant deformation reactions in actuators, the majority of light-responsive actuators are made using the photothermal actuation mode, which exhibits good stability, controlled reconfiguration, and outstanding performance.[10] The main tactics are to create high-performance actuators and intelligent soft actuators that react to external light stimuli. An intriguing option for multi-responsive and perhaps high-performance actuators is MXenes.[11–14] Through volume shrinkage brought about by water evaporation, the trilayered photothermal actuators with a cooling layer additionally improve the actuation performance.[12] Researchers discovered the MXene $Ti_3C_2T_x$, which shows broad absorption across the solar spectrum and high photo-thermal conversion efficiency and is currently in the research spotlight of advanced photo-actuation flexible materials, among other photothermal nanomaterials like carbon nanomaterials, gold nanoparticles, *etc.*[13] The GO-Au nanorods/polydimethylsiloxane (PDMS) based bilayer that makes up the soft actuator device is used to demonstrate the actuators versatility and adaptability in meeting various operational needs.[14] The main categories of light-driven actuations found in energy conversion schemes are photothermal, photochemical, photomechanical and photoelectronic actuations, which use heat, chemical, and electric energy as the intermediate stimuli, respectively.[15,16] A lot of work has been reported on constructing different light-responsive materials and flexible actuators.[17,18] Among many engineering materials, PEDOT:PSS based versatile materials are ideal for many applications including biomedical and bioelectronics.[19,20] It is a conducting polymer that has been considered as one among the most effective

[a] *Department of Physics and Electronics, Christ University, Bangalore, 560029, India. E-mail: partha.kumbhakar@christuniversity.in*
[b] *Department of Chemistry, Christ University, Bangalore, 560029, India*

† Electronic supplementary information (ESI) available. See DOI: https://doi.org/10.1039/d5ma00329f

thermoelectric polymers because of its useful applications. Compared to other polymers, PEDOT:PSS exhibits a broad light absorption behaviour.[21] However, PEDOT:PSS needs further improvement in terms of stretchability, stability and flexibility for different flexible optoelectronic applications.[22–25] Therefore, polymer mixing with two-dimensional (2D) materials is a simple and emerging process for preparing the stretchable and free-standing flexible devices. Recently, due to their remarkable mechanical, electrical, and optical qualities, 2D materials have attracted a lot of attention and have been widely used in sensors and actuators. Transition metal dichalcogenides (TMDs) are a novel class of 2D nanomaterials that have garnered a lot of interest because of their exceptional qualities, such as their high strength, tunable bandgap, and superior optical characteristics. Among other 2D families including carbonaceous materials, dichalcogenides, phosphides, nitrides and halides, MoS_2 has garnered increasing interest lately due to its unique layer dependent physical and electrical characteristics.[26,27] MoS_2 has good photothermal conversion properties. Covalently bound S–Mo–S monolayers are stacked *via* weak van der Waals interactions to generate the layered crystal structure of MoS_2, which helps in making a great filler for a polymer matrix composite. These layers can be separated because of the van der Waals interaction, which results in the exfoliation with a minimum thickness of about 0.65 nm. Optical and electrical characteristics are influenced by the layer number of MoS_2 and it shows broad absorption from the UV to the NIR region. One of the most attractive properties of a photothermal actuator is its ability to transform light energy into thermal energy. However, there are still a number of issues with layered MoS_2, such as restacking due to high surface energy, which can reduce the electrical conductivity, and photothermal properties under different light sources (visible and NIR light).[28] The aforementioned disadvantages can be addressed by hybridizing 2D materials with other conducting polymers for light stimulated soft actuators for smart applications. Therefore, making composites with MoS_2 and PEDOT:PSS can be a good solution for various soft actuation applications such as photothermal actuation, solvent vapor actuation, *etc*.[29,30] As a photothermal transduction agent, MoS_2 nanosheets allow for precise and distant actuator movement control. Soft robots are highly desired for these special physicochemical properties of 2D materials, which allow them to operate in many situations and react instantly to provide the best possible interactions between robots and humans. However, a major obstacle to fully utilizing their inherent physicochemical capabilities in the manufactured soft robots has been the incompatibility of ''hard'' 2D materials with ''soft'' matter. We concentrated on the enhanced capabilities of the resulting 2D materials and the potential uses of soft matter composites as novel multipurpose robotic skins or bodies.

In this paper, we propose a light driven photothermal actuator using a 2D MoS_2 and PEDOT:PSS based composite film (denoted as the MPS film) and study the effect of PEDOT:PSS in the actuation of the MoS_2 film. This prepared MPS film is used to study the actuation under NIR light. The variations in the materials' coefficients of thermal expansion create asymmetric strain, which is the actuation mechanism of the MPS films. The light-to-thermal conversion capabilities of the composite film show good actuation under NIR light-stimulation with a high response time. The photothermal property made it possible for effective shape deformation motions. The flexible NIR-responsive soft actuator based on few-layered MoS_2 and PEDOT:PSS is demonstrated in this work. It has several advantages, including flexibility, high sensitivity, compliance, and security. The manufactured MPS-based actuator exhibits several actuations, when the film is subjected to an NIR light source.[31,32] When the NIR is turned on, the MPS activates, and when the NIR is shut off, it reverts to its initial state. In addition, we used MPS to create a ''soft insect'' that is inspired by nature. The use of soft robotics in smart devices may be accelerated by the ongoing research on photothermal composite materials.[33,34]

Experimental

Chemicals

All the chemicals and solvents were utilized exactly as received and were of analytical quality. Bulk-layered MoS_2 (purity 99%), PEDOT:PSS and PVDF (purity 99%) powders were purchased from Sigma Aldrich.

Liquid exfoliation of MoS_2 nanosheets and preparation of the MPS film

MoS_2 nanosheets were synthesized using the liquid phase exfoliation method. Usually, 4 mg of powdered MoS_2 was added to 5 mL of DMF. After that, 1 mL of PEDOT:PSS solution was mixed with 1 mL of DMF. Later, 5 mL of PVDF solution and 2 mL of MoS_2 were mixed, sonicated for 2 hours, and then allowed to be magnetically swirled for another 2 hours. Additionally, to make the MPS film, PEDOT:PSS and MoS_2 were successively deposited on the substrate in strip form. Furthermore, different PEDOT:PSS and MoS_2 concentrations were utilized to make MPS1, MPS2 and MPS3-composite films. We have used MoS_2 and PEDOT:PSS to prepare the composite MPS film. The concentration of MoS_2 is kept constant whereas the concentration of PEDOT:PSS is varied. The ratios are MPS-1 with a 1 : 1 ratio with 0.9 wt%, MPS-2 with a 2 : 1 ratio with 1.03 wt%, and MPS-3 with a 3 : 1 ratio with 1.1 wt% PEDOT:PSS. Fig. S1, ESI† illustrates the steps involved in the synthesis of the PEDOT:PSS and MoS_2 composite for creating bilayer plasmonic actuators.

Characterization

UV-Vis absorption spectra were recored using a spectrophotometer (PerkinElmer, Lambda 30). Raman spectroscopy (Renishaw in-Via Raman Microscope) was carried out to verify the number of layers and defects of MoS_2 nanosheets. The microstructure of MoS_2 was characterized using transmission electron microscopy (TEM). The morphology of the film was examined using a scanning electron microscope (SEM), ThermoFisher (Apreo S LoVac), attached to an energy dispersive spectrometer (EDS). FTIR was carried out using a SHIMADZU IR-Prestige-21. A thermal imaging

camera (FLIR TOOLS E-50) was used to determine the temperature difference in the sample and to provide the visual image.

Results and discussion

Preparation and characterization of bilayer soft-actuators

The construction of the PEDOT:PSS/MoS_2-composite actuator is shown schematically in Fig. 1, along with the actuation characteristics of the actuator when subjected to near-infrared (NIR) light. The solution casting technique was used to fabricate the self-supporting MPS film, as discussed in the experimental section. The digital photograph of the fabricated MPS film is shown in Fig. 2(a), which shows good flexibility. The MPS film with bilayer structure was obtained by depositing the PEDOT:PSS on the MoS_2 film (see Fig. S1, ESI†). The flexibility of the bilayer film is demonstrated by its ability to be bent and folded Fig. 2(b) displays the cross-sectional SEM image of the MPS film; the bilayer structure is tightly bonded. The inset shows the schematic of the bilayer film, where the upper surface is PEDOT:PSS and the bottom surface represents 2D MoS_2. The thickness of the photoactive layer (PEDOT:PSS) of the MPS film is $\sim 60 \pm 4$ μm measured using ImageJ software. Light absorption on the material can result in significant deformation of a reasonably thin bilayer due to the characteristics of the chosen materials and the design of the actuators. Moreover, the MPS film characterized structure shows several layers as a result of the free deposition at varying PEDOT:PSS concentrations on the MoS_2 film. With the thinness of the active layer, the material shows an excellent actuating property, such that the small contraction can cause a bending displacement because of the thin bilayer MPS film. Hence, the stacked layer microstructure is useful for actuation. Fig. 2(c) shows the surface morphology (top view) of the MPS film. We observed similar-sized spherical PEDOT:PSS particles of size ~2.8 ± 0.2 μm. The round spheres are distributed on the surface of the MPS film. The high π electron density often achieved for conjugated conducting polymers is indicated by the particles' sharp contrast.[35] The inset of Fig. 2(c) shows the

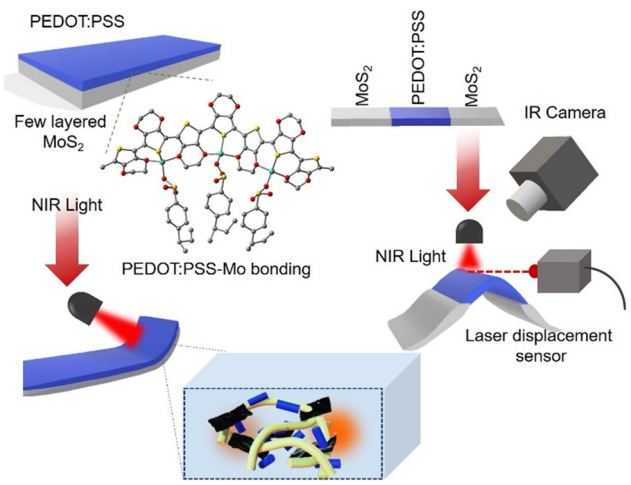

Fig. 1 Schematic representation of actuation under NIR light of the MPS composite film.

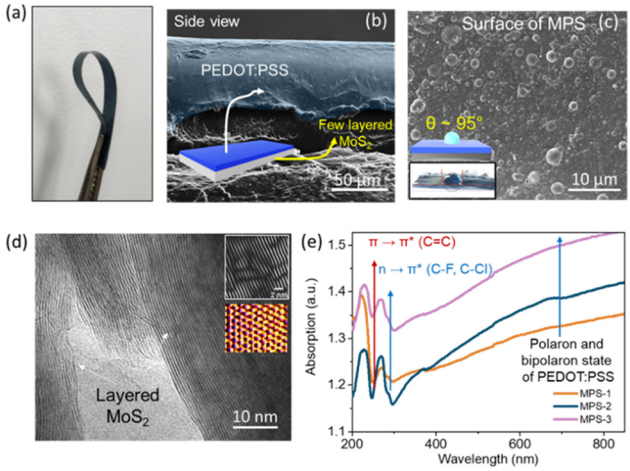

Fig. 2 (a) The optical image of the film. (b) SEM image of the bilayer MPS film in cross-section form. (c) Surface image of the MPS-3 (higher concentration of PEDOT:PSS) film; the inset shows the hydrophobic nature of the MPS film. (d) HRTEM image of multi-layered MoS_2. Inset shows the FFT pattern of the sheets. Lower inset shows the 3D atomic arrangement of MoS_2. (e) UV-vis absorption spectra of MPS films for various concentration ratios.

hydrophobicity of the film with a contact angle of ~95° and the water droplet stays on the top of the MPS film same after 5 min. Transmission electron microscopy with high resolution (HRTEM) presented here shows the many layers of MoS_2 that overlap and are comparatively flat and wrinkle-free sheets of the nanometre scale, Fig. 2(d). The top inset shows the fast Fourier transform (FFT) pattern of MoS_2 and confirms the surface defects on the sheets; the distortion in the arrangement of the stacked layers was observed. Surface topography configuration in 3D format (using ImageJ software) is shown in the bottom inset of Fig. 2(d), which confirms the presence of atomic defects in MoS_2 sheets.

To study the optical properties, the UV-visible absorption spectra of the three MPS films were taken and are shown in Fig. 2(e). As the ratio of the PEDOT:PSS concentration increases, no obvious spectral shift was seen, but the absorbance intensity increases throughout the entire range (UV to NIR).[36,37] A wider shoulder at lower wavelengths (250–280 nm) is caused by the PSS benzene ring π–π* transition.[30] The peak at ~290 nm (marked with an arrow) is allocated to the n–π* change in the PEDOT backbone.[38] Above 310 nm, PSS exhibits no absorption; instead, the PEDOT moiety provides the spectral response. Notably, depending on its intended use, the MoS_2-PEDOT:PSS composite concentration can be changed. The broad features in the absorption spectra above 400 nm can be interpreted as the absorption contribution from free charges. A different explanation for this absorption at a long wavelength and the wide feature is connected to the polaron or bipolaron states.[39] With the increase in PEDOT:PSS concentration the increased optical absorption and hydrophobic surface of the bilayer actuators demonstrate their application for real world scenarios. The theoretical study also confirms the actuation property of the MPS film as discussed later. FTIR spectra also confirm the arrangement of bonding between MoS_2 and PEDOT:PSS (Fig. S2, ESI†).

Photothermal properties of bilayer MPS actuators under NIR light

To investigate the impact of PEDOT:PSS on the photothermal properties of the MPS film, NIR light was used as the light source. Here, we have used NIR light of power density ~0.42 mW cm^{-2}, where the wavelength of the light is ~650 nm. We cut the strips with a dimension of length = 3 cm and width = 1 cm to get the light-responsive actuation of the film when exposed to NIR light. The schematic of experimental measurement is shown in the inset of Fig. 3(a). Both ends of the MPS film were connected across the Multimeter (Model No. METRAVI PRO-27) to check the electrical properties of the film using metal electrodes (Fig. S3, ESI†), which were fixed on the glass. The variation of resistance change (ΔR) was observed in Fig. 3(a), in relation to the duration of being exposed to light. After turning on the NIR light, the surface temperature (measured using a thermal camera, FLIR Tools: E-50) of the irradiated part rises and the surface resistance increases accordingly. Due to the presence of PEDOT:PSS in the MoS_2 film, the NIR light absorption increased and it was feasible to specifically excite the charge carriers. This causes the resistance to shift; however, the energy provided by the photons will be rapidly wasted due to the rapid thermalization of the carriers under NIR light and ΔR with time (Fig. S4, ESI†). Consequently, based on the carrier thermalization time, we found variation of surface resistance (or conductivity) when the film was exposed to NIR light (Fig. 3b and c). Interestingly the introduction of PEDOT:PSS into the MoS_2 matrix imparts high light responsiveness. The following formula describes the temperature-dependent conductivity of PEDOT:PSS thin films.[40]

$$\sigma(T) = \sigma_0 \exp[-(T_0/T)^{\alpha}] \quad (1)$$

where T_0 is the characteristic temperature and σ_0 is the conductivity pre-factor. As carriers are thermally activated, they hop between localized states at various energies. The exponent α is associated with the transport process.[41] In Fig. 3(b), we present the $\ln(\sigma)$ *vs.* $T^{-1/4}$ plot, which shows linear behaviour. Here, the Mott variable-range hopping (MVRH) model governs the charge transfer in PEDOT:PSS (for more details see ESI†). According to this model, charge carriers move between nearby localized states with varying energies. Furthermore, the change in temperature under NIR radiation was recorded using an IR camera for different intensities of light as depicted in Fig. 3(d and e) and Fig. S4 (ESI†). It shows a temperature increase from room temperature (30 °C) to 67 °C at 0.42 mW cm^{-2} within 20 seconds (Fig. S5, ESI†). In a similar way, the temperature is about 49 °C at a lower light intensity of 0.21 mW cm^{-2}. As a result, the temperature fluctuates more at greater intensities as the MPS film is activated. The only MoS_2 film is not light responsive as shown in (Fig. S6, ESI†). This illustrates that the NIR light causes the MPS film to excite more charge carriers, raising the MPS film temperature. Here PEDOT:PSS was observed to be one of the maximum promising options for resolving the crucial problems of MoS_2 nanosheet aggregation and precipitation because of the hydrophilic nature of its charged and active surface groups ($-SO_3H$ and $-SO_3^-$) as discussed later.[22]

We have studied the durability and stability of the actuators under NIR light exposure and the results are included in the revised manuscript. We have performed the durability test and measured the variation of temperature (light ON and OFF conditions) for 500 cycles (Fig. 3f), in which the inset shows the stability for 10 cycles with variation in temperature along with the actuation of the film under NIR light.

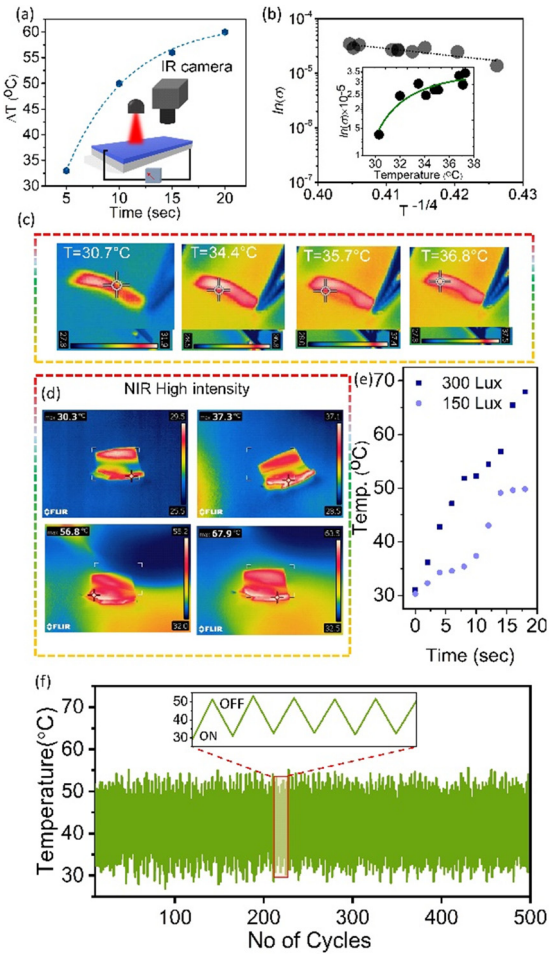

Fig. 3 (a) Variation of temperature under NIR exposure. Inset shows the schematic of the measurement. (b) The conductive test of the MPS film under NIR light and response time of the MPS film conductive material to change over time when exposed to NIR light. (c) Thermal images show the variation of temperature under NIR captured by an IR camera of the MPS film. (d) IR image of various light intensities. (e) The variation of temperature with time at different light intensities. (f) The stability of the MPS film for multiple cycles.

NIR light controlled actuation and its applications

Taking advantage of high conductivity and photothermal actuation properties, we designed MPS film-based strips. The temperature variation of MoS_2 and MPS sides is shown in Fig. 4(a), when NIR light is irradiated on the MPS composite and pristine MoS_2; variation in increase in temperature was seen on the MPS film from room temperature 27 °C to 75 °C, as PEDOT:PSS acts as the active material.[42] The area of the illuminated spot was ~15.89 cm^2 (where the radius of the area, r = 2.25 cm).

The distance between the lamp and the sample was kept at ~7 cm. Under a similar experimental configuration, when NIR light falls on the MPS film, the film is bent upward toward the light source. It is worth noting that the power density of NIR light used here was approximately 0.42 mW cm^{-2} and was kept constant throughout the experiment. Upon turning off the light source, the film gradually reverted to its original flat shape. The mechanism behind the light-derived actuation of these films is indirectly related to the remarkable photothermal conversion efficiency (PCE). In addition to the photothermal material's ability to absorb light, another crucial component is its efficiency in converting light into heat, which quantifies the absorbed energy transferred to thermal energy rather than re-emitting photon radiation. To determine the conversion efficiency, one must measure the temperature rise and compute the amount of heat produced by the incident light. The efficiency of photothermal conversion (η) can be calculated using the given equation,

$$\eta = \frac{\text{output energy}}{\text{input energy}} \times 100\% \quad (2)$$

It was determined that the overall energy efficiency from NIR light radiation to photothermal film actuation was almost ~20% (for more details, see ESI†). The benefit of this approach is that the photothermal material only generates thermal energy from the absorbed photons. Since the amount of heat produced is dependent on the amount of photothermal material used, it is difficult to compare the efficiency ratings of different materials directly using this method.[43] The infrared thermal image of the MPS film is shown in Fig. 4(b). Upon exposing the NIR light, the MPS film shows the actuation, and the temperature of the irradiated part increases, *i.e.*, the PEDOT:PSS part of the film, but the temperature of the other part of the strip hardly changes. Fig. 4(c and d) shows the rolling and twisting of the MPS thin film under NIR light radiation (Video S1, ESI†), and no actuation was observed under visible light. Energy conversion techniques are frequently used by NIR light responsive actuators to ultimately accomplish the goal of mechanical deformation. Thus, under NIR light the MPS film experiences photothermal deformation, which enables it to bend quickly and reversibly. Using the laser displacement sensors (Model No. optoNCDT 1220) depicted in Fig. 4(e), we were able to determine the displacement of the film Δh, which came out to be approximately 8.3 mm. We have estimated the response time of the deformation (bending starting) and it is found to be ~2–3 seconds (Video S2, ESI†). The PEDOT:PSS strip actuates when the NIR is turned on, and it returns to its initial condition when the NIR is off. Furthermore, we have designed a "soft insect" using the MPS, drawing inspiration from natural life. The actuation of the "soft insect" upon switching the NIR light on and off is depicted in Fig. 4(f). The self-adaptive resistance change allows the device arm to be controlled by NIR light, and its mobility can be tracked in real time. The bending of legs of the insect is due to the photothermal effect of the MPS film (the right inset of Fig. 4f). Furthermore, we have studied the comparison of the actuation properties (light stimulus-based) of 2D materials as tabulated in the ESI† (Tables S1 and S2). It shows that the fabricated MPS actuators show significant actuation behaviour compared to the other materials.

To study the actuation mechanism of the MPS film, we have performed the *in situ* Raman measurement. Raman spectroscopy is a useful tool for studying symmetric bonds, such as C–C bonds, and is used to identify conducting polymers and carbon compounds.

Here, it was employed to identify the temperature-induced structural change in the PEDOT:PSS molecule. Fig. 5(a) illustrates how temperature affects the π-conjugated structural change during NIR light exposure on the molecular conjugated structure. The vibrational modes of PEDOT are ascribed to the

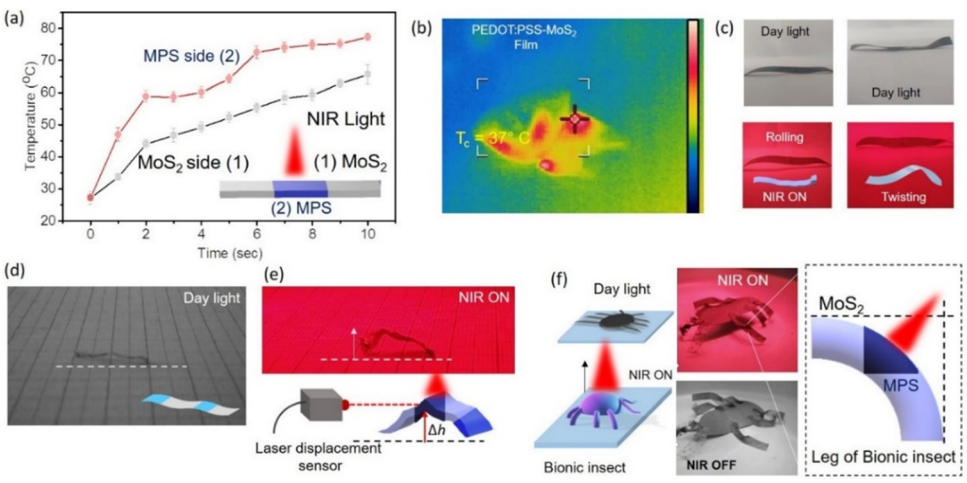

Fig. 4 (a) Graph explains the variation of temperature for two different spots of the film under NIR light along with the schematic of the MPS film under NIR light. (b) The thermal image of the MPS film, under NIR light. (c) Digital images represent the actuation (rolling and twisting) of the MPS film under NIR on–off conditions. (d) and (e) Digital image of the actuation property (bending upward) of the film under NIR light exposure. Lower inset shows the variation of displacement and it was measured using a laser displacement sensor. (f) Bio-inspired "soft insect", which shows the soft actuation property under NIR light exposure. Digital image of the soft insect under visible and NIR light.

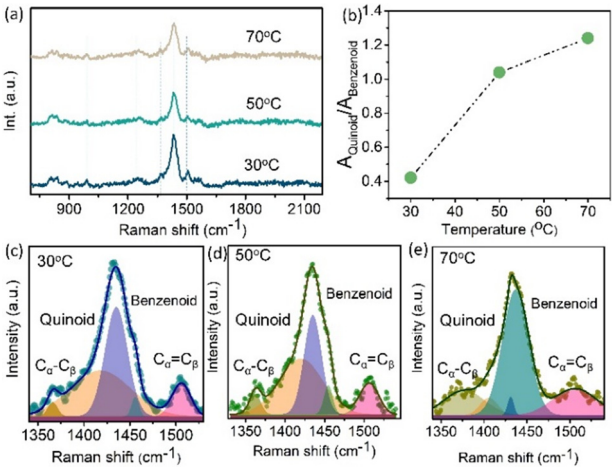

Fig. 5 (a) Raman spectra of PEDOT:PSS films at various temperatures between 30 °C and 70 °C after exposure to NIR light. (b) Quinoid and benzenoid structural transition trend. (c)–(e) The deconvoluted Raman spectra at various temperatures when MPS is exposed to NIR light.

C_α═C_β symmetrical, C_α═C_β asymmetrical, C_β–C_β stretching, and C_α–$C_{\alpha'}$ stretching vibrations between rings correspondingly and are found at 1524 cm^{-1}, 1452 cm^{-1}, 1383 cm^{-1}, and 1221 cm^{-1}. PSS has two vibrational modes, which are at 980 cm^{-1} and 850 cm^{-1}.[44] A Raman shift occurs when the film is exposed to NIR light; we have seen this shift for temperatures ranging between 30 °C and 70 °C. When the temperature increases, the intensity of the matching PEDOT band gradually reduces. However, as shown in Fig. 5(b), the ratio of the content of the Quinoid structure progressively decreases as the temperature goes higher. The chemical structure of the MoS_2 and PEDOT:PSS film is as follows: PSS connects by electrostatic interaction with the PEDOT backbone, and PEDOT is a conductive polymer based on thiophene that contains units of ethylene glycol replaced at the 3 and 4 positions. Two distinct conjugated structures—benzenoid (neutral) and quinoid (polaron)—generally make up the PEDOT backbone. Because of their almost identical orientations, adjacent thiophene rings in the quinoid structure nearly produce the delocalization of π-electrons throughout the PEDOT chain. But in the benzenoid structure the thiophene ring resembles a σ-bond more than anything else, and the π-conjugated electron density is smaller and more confined on PEDOT molecules than in the quinoid structure (C_α═C_β) where the carbon atoms are at α and β locations in the ring of thiophene.

The quantitative analysis of the resonance structure transition of the PEDOT molecular structure is shown in Fig. 5(c–e), where various Raman spectra were deconvoluted. The bands were revealed by the deconvolution in the Raman spectra. Both the benzenoid and quinoid compounds changed with respect to temperature. The amount of quinoid structure increased gradually as the temperature increased.

The PEDOT:PSS is primarily stabilized through electrostatic interactions, steric hindrance, and a balance between hydrophilic and hydrophobic forces. The positively charged PEDOT chains are electrostatically stabilized by the negatively charged sulfonate ($-SO_3^-$) groups of PSS, preventing aggregation. Additionally, the long PSS chains provide steric hindrance, enhancing solubility and dispersion in aqueous and polar media. The hydrophilic nature of PSS facilitates water dispersibility, while its interaction with the hydrophobic PEDOT ensures overall stability, Fig. (6a). Furthermore, hydrogen bonding and π–π interactions contribute to the structural integrity of the complex, maintaining its colloidal stability and conductive properties.

To describe the process by which PEDOT-PSS binds to the metal ion Mo, we have performed Molecular Electrostatic Potential (MEP) analysis of PEDOT:PSS and the structural optimization of the PEDOT–Mo complex using DFT calculations at the B3LYP level (Fig. 6) (see ESI† for more details). The 6-31G(d,p) Gaussian 09 was used to make the computations. The PEDOT-PSS basis set was employed, and the metal complex was based on the LANL2DZ basis set. To investigate the metal complex formation of PEDOT-PSS with molybdenum (Mo), molecular electrostatic potential (MEP) analysis was performed to identify potential metal binding sites. The MEP surface is a crucial tool for understanding the physicochemical properties and molecular structure of PEDOT-PSS.[45] It provides valuable insights into the nucleophilic and electrophilic (negative) and (positive) regions, revealing information about size, shape,

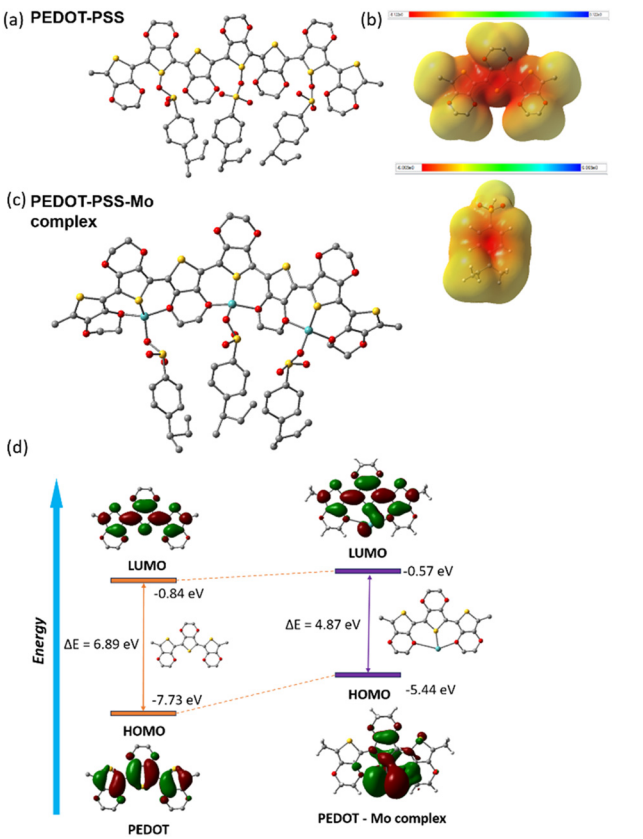

Fig. 6 (a) Gauss structure of PEDOT:PSS. (b) Molecular electrostatic potential (MEP) of PEDOT (left) and PSS (right). (c) Gauss structure of the PEDOT-PSS with Mo complex. (d) Energy optimized structures of PEDOT and the PEDOT with Mo complex.

charge distribution, and electronegativity. The MEP surface utilizes different colours to represent variations in the electrostatic potential; green indicates neutral areas, blue indicates positive ones, while red indicates negative electrostatic potential. The electrostatic potential of the PEDOT molecule ranges from −8.122 a.u. to +8.122 a.u., while for PSS, it ranges from −6.069 a.u. to +6.069 a.u, with a matching colour gradient that changes from red to blue (Fig. (6b)).[46]

The stabilization of the Mo complex with PEDOT was further confirmed through the optimization of the PEDOT and PEDOT–Mo complex structures (Fig. 6c). The calculated HOMO–LUMO energy gap for PEDOT was found to be 6.89 eV (HOMO = −7.73 eV, LUMO = −0.84 eV), whereas for the PEDOT–Mo complex, it was reduced to 4.87 eV (HOMO = −5.44 eV, LUMO = −0.57 eV) (Fig. 6(d)). From the optimized structure of the PEDOT–Mo complex, the calculated bond distances between Mo and the sulfur and oxygen atoms of PEDOT are 2.18 Å and 3.01 Å, 2.38 Å, in turn. The bond angles between Mo and the sulphur and oxygen of PEDOT are calculated as 69.06° and 76.99° respectively. Consequently, the significant reduction in the HOMO–LUMO energy gap upon Mo binding suggests enhanced stabilization of the PEDOT–Mo complex. Additionally, the molecular electrostatic potential (MEP) analysis reveals substantial electrostatic potential distribution, further supporting the stabilization of the PEDOT–Mo complex. Moreover, the PEDOT–Mo complex exhibits a notable spatial separation of frontier molecular orbitals (FMOs). The HOMOs are primarily localized on the metal center, while the LUMOs are predominantly distributed along the PEDOT–Mo complex, influencing its interaction with PSS. Molybdenum binds between PEDOT and PSS through four-coordinate bonding, involving interactions with sulfur and two oxygen atoms from PEDOT, as well as one sulfonate oxygen, forming the PEDOT-PSS–Mo complex, Fig. 6(c). The PEDOT-PSS–Mo complex exhibits responsiveness to near-infrared (NIR) light due to electronic transitions present in the PEDOT:PSS complex as shown in the UV-vis absorption graphs of the films. Specifically, the $S_0 \rightarrow S_2$ transition (excitation energy: 1.94 eV, oscillator strength (f) = 0.0015) corresponds to an absorption band at ∼639.41 nm, while the $S_0 \rightarrow S_4$ transition (excitation energy: 1.97 eV, oscillator strength (f) = 0.001) corresponds to an absorption band at 628.94 nm. These theoretical computations align well with experimental results, where a broad absorption band appears at wavelengths above 500 nm. Therefore, the formation of the PEDOT-PSS–Mo complex helps to absorb the NIR light, showing actuation behaviour.

Conclusions

In conclusion, we present a flexible NIR light-driven soft actuator based on MoS_2/PEDOT:PSS composites. Upon NIR light exposure, the fabricated MPS based actuator shows different actuation behaviours such as bending, rolling and twisting deformation. The distinctive characteristics of MoS_2/PEDOT:PSS are demonstrated by both the surface conductivity and actuation properties. The *in situ* Raman spectroscopy results of the MPS film demonstrate the impact of structural transition in a transparent manner from quinoid to benzenoid of PEDOT under NIR light intensity. The DFT calculation further confirms the formation of the PEDOT-PSS–Mo complex and its photo-thermal response. We also designed a nature inspired ''soft insect'' and it shows the NIR-responsive actuation with good response time. Therefore, we believe that the current work on photothermal composite materials could accelerate the soft-robotics applications in smart devices.

Data availability

The data supporting this article have been included as part of the ESI.†

Conflicts of interest

There are no conflicts to declare.

Acknowledgements

R. D. S. and P. K. are grateful for the financial support from Science and Engineering Research Board (currently ANRF), India, for the sponsored project *via* SRG grant (SRG/2023/001763) and Christ University for providing research facilities (Seed Project No: SMSS-2328).

References

1 S. Ma, X. Li, S. Huang, J. Hu and H. Yu, *Angew. Chem., Int. Ed.*, 2019, **58**, 2655–2659.
2 S. Wu, Y. Hong, Y. Zhao and Y. Zhu, *Sci. Adv.*, 2023, **9**, eadf8014.
3 D. Chen and Q. Pei, *Chem. Rev.*, 2017, **117**, 11239–11268.
4 P. Kumbhakar, S. Narendhiran, S. Midya, M. Islam, M. Balachandran and A. K. Singh, *Adv. Mater. Technol.*, 2025, **10**, 2401037.
5 L. Zhang, G. Bao, Q. Yang and F. Gao, *China Mech. Eng.*, 2008, **19**, 2891–2897.
6 A. D. Greef, P. B. Lambert and A. Delchambre, *Precis. Eng.*, 2009, **33**, 311–321.
7 E. Kopperger, J. List, S. Madhira, F. Rothfischer, D. C. Lamb and F. C. Simmel, *Science*, 2018, **359**, 296–301.
8 L. Hines, K. Petersen, G. Z. Lum and M. Sitti, *Adv. Mater.*, 2017, **29**, 1603483.
9 M. Pd Cunha, M. G. Debije and A. P. H. J. Schenning, *Chem. Soc. Rev.*, 2020, **49**, 6568–6578.
10 Z. Yin, F. Yuan, M. Xue, Y. Xue, Y. Xie, J. Ou, Y. Luo, Z. Hong and C. Xie, *J. Colloid Interface Sci.*, 2022, **611**, 93.
11 G. Cai, J. Ciou, Y. Liu, Y. Jiang and P. S. Lee, *Sci. Adv.*, 2019, **5**, eaaW 7956.
12 J. Li, R. Zhang, L. Mou, M. J. d Andrade, X. Hu, K. Yu, J. Sun, T. Jia, Y. Dou, H. Chen, S. Fang, D. Qian and Z. Liu, *Adv. Funct. Mater.*, 2019, **29**, 1808995.

13 M. Yang, Y. Xu, X. Zhang, H. K. Bisoyi, P. Xue, Y. Yang, X. Yang, C. Valenzuela, Y. Chen, L. Wang, W. Feng and Q. Li, *Adv. Funct. Mater.*, 2022, **32**, 2201884.
14 K. Li, Q. Zhang, X. Cui, Y. Liu, Y. Liu and Y. Yang, *Chem. Eng. J*, 2024, **498**, 155057.
15 F. Ilievski, A. D. Mazzeo, R. F. Shepherd, X. Chen and G. M. Whitesides, *Angew. Chem.*, 2011, **123**, 1930–1935.
16 X. Liu, R. Wei, P. T. Hoang, X. Wang, T. Liu and P. Keller, *Adv. Funct. Mater.*, 2015, **25**, 3022–3032.
17 Z. Cai, Z. Song and L. Guo, *ACS Appl. Mater. Interfaces*, 2019, **11**, 12770–12776.
18 P. Zhang, B. Wu, S. Huang, F. Cai, G. Wang and H. Yu, *Polymer*, 2019, **178**, 121644.
19 B. Lu, H. Yuk, S. Lin, N. Jian, K. Qu, J. Xu and X. Zhao, *Nat. Commun.*, 2019, **10**, 1043.
20 J. Li, J. Cao, B. Lu and G. Gu, *Nat. Rev. Mater.*, 2023, **8**, 604–622.
21 P. Wilson, C. Lekakou and J. F. Watts, *Org. Electron.*, 2012, **13**, 409–418.
22 Y. H. Kim, C. Sachse, M. L. Machala, C. May, L. M. Meskamp and K. Leo, *Adv. Funct. Mater.*, 2011, **21**, 1076–1081.
23 Y. Xuan, M. Sandberg, M. Berggren and X. Crispin, *Org. Electron.*, 2012, **13**, 632–637.
24 N. A. A. Shahrim, Z. Ahmad, A. W. Azman, Y. F. Buys and N. Sarifuddin, *Mater. Adv.*, 2021, **2**, 7118–7138.
25 C. O. R. Quiroz, G. D. Spyropoulos, M. Salvador, L. M. Roch, M. Berlinghof, J. D. Perea, K. Forberich, L. I. D. Bertrand, N. J. Schrenker, A. Classen, N. Gasparini, G. Chistiakova, M. Mews, L. Korte, B. Rech, N. Li, F. Hauke, E. Spiecker, T. Ameri, S. Albrecht, G. Abellan, S. Leon, T. Unruh, A. Hirsch, A. Aspuru-Guzik and C. J. Brabec, *Adv. Funct. Mater.*, 2019, **29**, 1901476.
26 K. K. Zadeh, J. Z. Ou, T. Daeneke, A. Mitchell, T. Sasaki and M. S. Fuhrer, *Appl. Mater. Today*, 2016, **5**, 73–89.
27 A. Sinha, Dhanjai, B. Tan, Y. Huang, H. Thao, X. Dang, J. Chen and R. Jain, *TrAC, Trends Anal. Chem.*, 2018, **102**, 75–90.
28 F. Jiang, J. Xiong, W. Zhou, C. Liu, L. Wang, F. Zhao, H. Liu and J. Xu, *J. Mater. Chem. A*, 2016, **4**, 5265.
29 L. V. Kayser and D. J. Lipom, *Adv. Mater.*, 2019, **31**, 1806133.
30 H. Okuzaki, H. Suzukia and T. Ito, *Synth. Met.*, 2009, **159**, 2233.
31 P. Xue, C. Valenzuela, S. Ma, X. Zhang, J. Ma, Y. Chen, X. Xu and L. Wang, *Adv. Funct. Mater.*, 2023, **33**, 2214867.
32 Y. Chen, C. Valenzuela, Y. Liu, X. Yang, Y. Yang, X. Zhang, S. Ma, R. Bi, L. Wang and W. Feng, *Matter*, 2025, **8**, 101904.
33 Y. Chen, C. Valenzuela, X. Zhang, X. Yang, L. Wang and W. Feng, *Nat. Commun.*, 2023, **14**, 3036.
34 S. Ma, P. Xue and Y. Tang, *Responsive Mater.*, 2024, **2**, e20230026.
35 J. Zhou, D. H. Anjum, L. Chen, X. Xu, I. A. Ventura, L. Jiang and G. Lubineau, *J. Mater. Chem. C*, 2014, **2**, 9903–9910.
36 J. Ouyang, X. Qianfei, C.-W. Chu, Y. Yanga, G. Li and J. Shinar, *Polymer*, 2004, **45**, 8443.
37 J. L. Bredas, F. Wudl and A. J. Heeger, *Solid State Commun.*, 1987, **63**, 577–580.
38 O. P. Dimitriev, Y. P. Piryatinski and A. A. Pud, *J. Phys. Chem. B*, 2011, **115**, 1357–1362.
39 R. Gangopadhyay, B. Das and M. R. Molla, *RSC Adv.*, 2014, **4**, 43912–43920.
40 O. P. Dimitriev, D. A. Grinko, Yu. V. Noskov, N. A. Ogurtsov and A. A. Pud, *Synth. Met.*, 2009, **159**, 2237.
41 A. M. Nardes, M. Kemerink, R. A. J. Janssen, J. A. M. Bastiaansen, N. M. M. Kiggen, B. M. W. Langeveld, A. J. J. M. V. Breemen and M. M. d Kok, *Adv. Mater.*, 2007, **19**, 1196–1200.
42 P. Zhou, J. Lin, W. Zhang, Z. Luo and L. Chen, *Nano Res.*, 2022, **15**, 5376–5383.
43 D. Wang, Z. Hou, F. Wang, H. Zhang, J. Jiang and B. Dong, *J. Mater. Chem. C*, 2024, **12**, 4453.
44 S. Guo, Y. Park, E. Park, S. Jin, L. Chen and Y. M. Jung, *Angew. Chem., Int. Ed.*, 2023, **62**, 6709.
45 M. Hagar, H. A. Ahmed, G. Aljohani and O. A. Alhaddad, *Int. J. Mol. Sci.*, 2020, **21**, 3922.
46 H. Gokce, F. Sen, Y. Sert, B. F. Abdel-Wahab, B. M. Kariuki and G. A. El-Hiti, *Molecules*, 2022, **27**, 2193–3014.